processes

MDPI

Article

The Prediction of Separation Performance of an In-Line Axial Oil–Water Separator Using Machine Learning and CFD

Yeong-Wan Je [1], Young-Ju Kim [2] and Youn-Jea Kim [3,*]

[1] Graduate School of Mechanical Engineering, Sungkyunkwan University, Suwon 16419, Korea; ywje@skku.edu
[2] Korea Research Institute of Geoscience and Mineral Resources, Pohang 37559, Korea; kyjp7272@kigam.re.kr
[3] School of Mechanical Engineering, Sungkyunkwan University, Suwon 16419, Korea
* Correspondence: yjkim@skku.edu

Abstract: Recently, global energy consumption has increased due to industrial development, resulting in increasing demand for various energy sources. Aside from the increased demand for renewable energy resources, the demand for fossil fuels is also on the rise. Accordingly, the demand for resource development in the deep sea is also increasing. Various systems are required to efficiently develop resources in the deep sea. A study on an in-line type oil–water separator is needed to compensate for the disadvantages of a gravity separator that separates traditional water and oil. In this paper, the separation performance of the axial-flow oil–water separator for five design variables (conical diameter, conical length, number of vanes, angle of vane, and thickness of vane) was analyzed. Numerical calculations for multiphase fluid were performed using the mixture model, one of the Euler–Euler approaches. Additionally, the Reynolds stress model was used to describe the swirling flow. As a result, it was found that the effect on the separation performance was large in the order of angle of vane, conical diameter, number of vanes, the thickness of vane, and conical length. A neural network model for predicting separation performance was developed using numerical calculation results. To predict the oil–water separation performance, five design parameters were considered, and the evaluation of the separation performance prediction model was compared with the multilinear regression (MLR) model. As a result, it was found that the R square was improved by about 74.0% in the neural network model, compared with the MLR model.

Keywords: in-line axial oil–water separator; swirl generator; separation efficiency; machine learning

Citation: Je, Y.-W.; Kim, Y.-J.; Kim, Y.-J. The Prediction of Separation Performance of an In-Line Axial Oil–Water Separator Using Machine Learning and CFD. *Processes* **2022**, *10*, 375. https://doi.org/10.3390/pr10020375

Academic Editors: Jin-Hyuk Kim, Sung-Min Kim, Joon Ahn, Lei Tan, Bin Huang and Ji Pei

Received: 3 January 2022
Accepted: 11 February 2022
Published: 16 February 2022

1. Introduction

Recently, due to the increase in worldwide energy consumption and the decrease in the production of fossil fuels (oil, gas, etc.) on land and offshore, the demand for resource development in the deep sea is increasing. Resource development in the deep sea was carried out in the 200 m depth in the early 1990s, but with the continuous development of exploration technology and resource plant technology, it has recently become possible to develop resources even at depths of over 3000 m. Traditionally mined crude oil was separated into solid, liquid, and gas phases by gravity separation. However, in the case of the deep sea, there is a limitation in using a traditional gravity separator having a relatively large volume. Due to the relatively large volume, there are limitations on the installation area and the need for a robust design to withstand high pressure. To improve on these shortcomings, research on in-line-type separators capable of efficiently separating in the deep sea is being actively conducted. In-line-type separators have the advantages of being used in the deep sea, as well as increasing production efficiency and enabling compact plant design.

The swirl generator is installed in the oil separator, and the working fluid is separated into water and oil with different densities through the swirl flow. Studies using swirl flow for multiphase separation are being actively conducted. Numerical calculations and

experimental studies on the separation performance of the gas–solid phase using a cyclone separator have also been conducted.

Wang et al. [1] conducted numerical analysis and experiments on particle behavior for a typical Lapple cyclone. The researchers conducted a numerical analysis using the Reynolds stress model and verified it through experiments. Chu et al. [2] calculated the effect of the various mass flow rate of particles flowing into the cyclone separator on pressure drop using the discrete element method (DEM). Klujszo et al. [3] analyzed the effect of various design parameters on dust collection performance by applying a fixed guide vane. Zhou et al. [4] analyzed the numerical and experiments on the behavior of ultra-light particles in a cyclone separator. In addition, a study on optimizing the configuration of a cyclone separator to increase the separation efficiency was conducted [5]. Mikulcic et al. [6] calculated numerically using the large eddy simulation (LES) for particle behavior. In the gas–liquid phase, Liu and bai [7] performed numerical analysis and experiments on the swirl decay in a straight pipe with a swirler applied. Xiong et al. [8] visualized the effect of the flow pattern on the flow characteristics in the separator through numerical experiments. Rocha et al. [9] studied the flow characteristics according to various Reynolds numbers. Hung et al. [10] analyzed the effect of various configurations of swirlers on flow characteristics through numerical analysis and experiments. Hreiz et al. [11] visualized the flow characteristics in the separator according to various shapes and boundary conditions. Swanborn [12] conducted a study of various separators used in the oil industry. Yue et al. [13] et al. performed numerical analysis and experiments on a gas–liquid cylindrical cyclone separator. Wang et al. [14] performed an experiment for flow characterization of a multistage separator. Liu et al. [15] observed the change in the swirling flow with time. In the liquid–liquid phase, Delfos et al. [16] compared the hydrocyclone axial averaged slice (HAAS) model and the commercial code (Fluent) results, and similar calculation results were found. Amini et al. [17] performed numerical calculations and experiments on separators of various configurations. In addition, the effect of oil droplet size and flow rate on efficiency was analyzed. The performance of the cyclone separator was analyzed through numerical calculations and experiments using a Reynolds stress model, which is excellent for anisotropic flow prediction [18,19]. Husveg et al. [20] experimented to analyze the effect of changing the flow rate on hydrocyclone performance. The experiments were conducted to validate the numerical calculation of the oil-water separator [21–24]. The effects of the various configurations of the separator and various boundary conditions of working fluid on the separation performance were analyzed [25–28]. In addition, optimization studies were conducted to improve the separation performance. Young et al. [29] and Al-kayiem et al. [30] conducted studies on the optimal design of the swirl generator. Zeng et al. [31] analyzed the effect of separator chamber geometry on separation performance. It was confirmed that the conical chamber was more effective for separation than the cylinder and diffuser chamber.

In this paper, a machine learning model study on the separation performance of an in-line oil–water separator was performed using computational fluid dynamics (CFD) results. Although relatively high cost is required for CFD calculation of various design parameters, machine learning has the advantage of efficiently calculating complex nonlinear mathematical models based on data. Machine learning, which has the advantages of efficient calculation, is also used in the field of predicting cyclone separator performance based on swirl flow. Elsayed and Lacor [32] accurately predicted complex nonlinear relationships between performance coefficients and design parameters and showed that it is a powerful approach to optimization for performance improvement. Safikhani [33] and Park et al. [34] conducted studies on improving separator performance through CFD results and various algorithm combinations. However, previous studies have focused on predicting gas–solid separation performance. Therefore, in this study, a machine learning algorithm was applied to the development of a predictive model for liquid–liquid separation performance using swirling flow. Figure 1 shows the flowchart of this study. First, based on the design-of-experiment (DOE) method, various design points for the swirl generator

were created. Next, CFD calculation was performed on the created design point, and a machine learning model was developed using the CFD calculation result data. Finally, the developed model evaluated the predictive performance, compared with the traditional, multilinear regression (MLR) model.

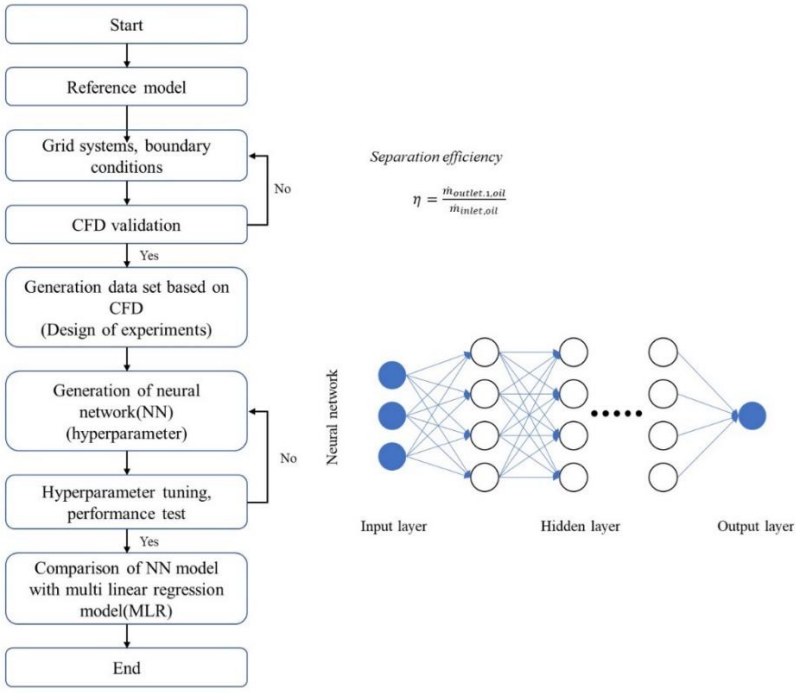

Figure 1. Research flowchart.

2. Model Description

Figure 2 shows the in-line oil separator used in this study. The total length of the oil–water separator was 2440 mm, and the swirl generator was installed 200 mm away from the inlet. The outer diameter (D) of the swirl generator was 100 mm, and the total length was 240 mm. Additionally, the swirl generator consisted of the nose section, the vane section, and the tail section, and they were 80 mm (L_{nose}), 80 mm (L_{vane}), and 80 mm (L_{tail}), respectively.

Figure 3 shows the grid system of the oil separator. The grid system was composed of polyhedrons and hexahedrons using ANSYS Fluent Meshing. The maximum and minimum sizes of the grid were set to 6 mm and 0.02 mm, respectively. The maximum skewness of the grid was 0.7, and the minimum orthogonal quality was 0.2. A scalable wall function was used as the near-wall treatment, and the y^+ value was set to $y^+ > 11$. The residual values of the turbulence equation and the separation efficiency criteria for evaluating CFD convergence were set to 10^{-3}, respectively. The number of grid elements was calculated by changing from 700,000 to 3,500,000, and as a result, the change in separation efficiency was insignificant from about 2,200,000 (Figure 4). The oil separator consisted of one inlet and two outlets for discharging oil and water. The boundary conditions for numerical calculation were defined as velocity inlet and outflow. The central and annulus outlets were set as outflow, with the central outlet flow split of 30%. The relatively heavy phase was pushed outward by centrifugal force, and the light phase was directed toward the center. Therefore, the annulus outlet was set as a heavy phase outlet (HPO) because the fluid of the relatively heavy phase exits, and the central outlet was set as the light phase outlet (LPO) because of the fluid of the relatively light phase exits. The volume fraction of the mixture flowing into the separator was set to 0.8 for water and 0.2 for oil. Additionally, a no-slip boundary condition was applied to all walls.

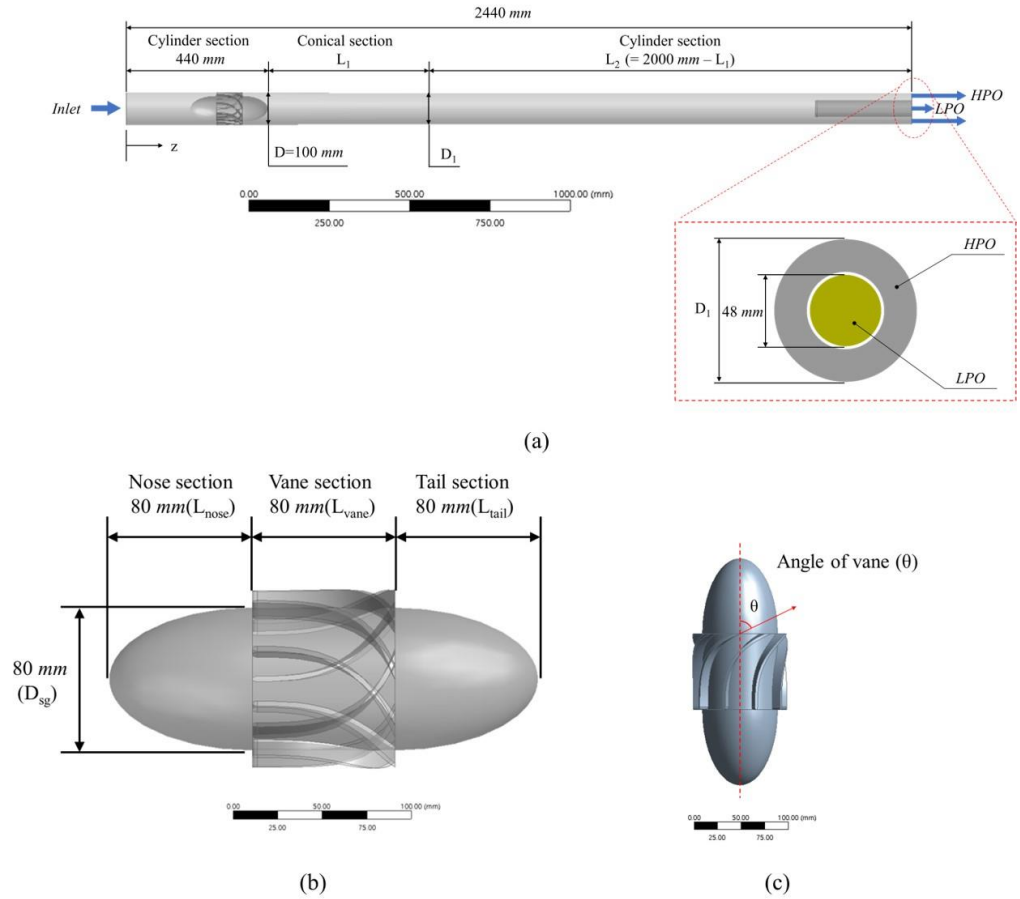

Figure 2. Schematic of the modeled in-line axial separator: (**a**) The schematic of the separator, (**b**) The schematic of the swirl generator, (**c**) The diagram of angle of vane.

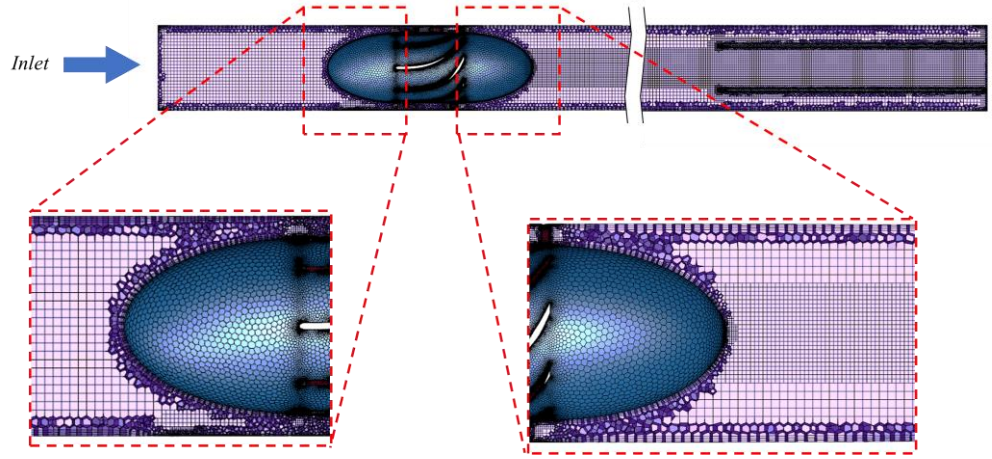

Figure 3. Grid systems.

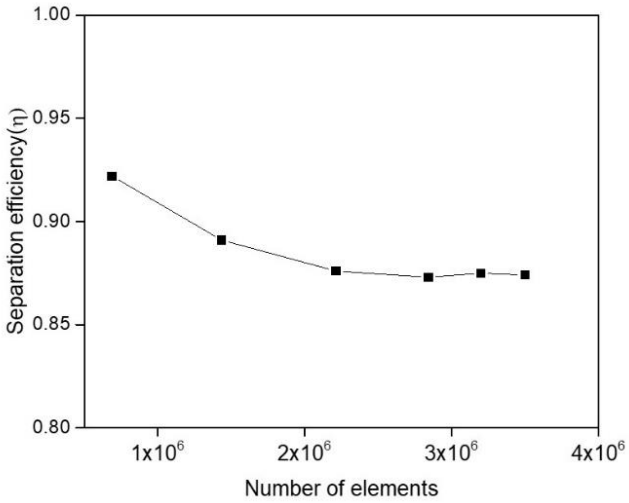

Figure 4. Grid dependency test.

In this study, a mixture model, one of the Euler–Euler approaches, was applied. the mixture model treats the different phases as interpenetrating continua and can completely capture the multiphase. The mixture model has been applied successfully on the simulation of oil–water separation [31,35,36]. and this model solves the momentum equation of the mixture and describes the discrete phases by relative velocity. The continuity and momentum equation can be represented as follows, respectively:

$$\nabla \cdot \left(\rho_m \vec{v}_m \right) = 0 \tag{1}$$

$$\begin{aligned} \nabla \cdot \left(\rho_m \vec{v}_m \vec{v}_m \right) = & -\nabla p + \nabla \cdot \left[\mu_m \left(\nabla v_m + \nabla \vec{v}_m^T \right) \right] \\ & + \rho_m \vec{g} + \vec{F} + \nabla \cdot \left(\sum_{k=1}^{n} \alpha_k \rho_k \vec{v}_{dr,k} \vec{v}_{dr,k} \right) \end{aligned} \tag{2}$$

where ρ_m is the mixture density, $\vec{v}_m$ is the mixture velocity, μ_m is the viscosity of the mixture, $\vec{g}$ is the gravity acceleration, $\vec{F}$ is the body force, α_k, and $\vec{v}_{dr,k}$ are the volume fraction and drift velocity for phase k, respectively.

Table 1 describes the physical properties of the mixture applied in this study and the boundary conditions for numerical calculation. The droplet size of the oil, defined as the dispersed phase, was set to 100 μm. For the drag law used in the momentum conservation equation, the Ishii–Zuber model [37] was applied. This drag law model is characterized by satisfactory agreement for bubble, droplet, and particle motion over a wide range of concentrations and Reynolds numbers. According to the literature on swirling flow, complex flows such as vortex breakdown, shortcut flow, circulation flow, etc. were observed [38,39]. To account for complex flows, the choice of turbulence model is important. Yang et al. [40] compared the numerical results using the Reynolds stress model (RSM) with the experimental data. As a result, their findings reveal that the turbulence model used was agreeable. Cai et al. [41] compared the numerical results of Equation (2) model (realizable k–ε, RNG k–ε, and k–ω SST) and Equation (7) model (RSM) and confirmed that the RSM model predicts the swirling flow well through experiments. Therefore, the RSM was applied in this study. Numerical calculations were performed using ANSYS Fluent. A workstation equipped with an Intel Xeon CPU process (@ 2.00 GHz, 14 core, X2 process) and 200GB RAM was used for calculations.

Table 1. Boundary conditions applied in this study.

				Value
Calculation type				Steady state
Turbulence model				Reynolds stress model
Working fluid	Water	Density $[kg/m^3]$		1068.7
		Viscosity $[kg/(m{\cdot}s)]$		1.183×10^{-3}
	Oil	Density $[kg/m^3]$		867
		Viscosity $[kg/(m{\cdot}s)]$		8.69×10^{-3}
		Droplet size $[\mu m]$		100
Gravity (z-axis) $[m/s^2]$				-9.81
Inlet	Velocity [m/s]			2
	Volume of fraction		0.8	(water 13.416 kg/s)
			0.2	(oil 2.730 kg/s)
Outlet	Flow split	LPO		0.3
		HPO		0.7
Wall				No-slip wall
Drag law				Ishii–Zuber model

3. Machine Learning Algorithm

CFD simulations that combine various geometrical design parameters have the disadvantage of being time consuming. In this paper, it took 20 h for each case to calculate the CFD and about 10 h to calculate the ML model development. A machine learning model for separation performance was developed for solving the time cost problem of oil–water separator design. This model was developed using a backpropagation algorithm that efficiently learns multilayer perceptron. The backpropagation model is a model with the advantage of minimizing the error by performing calculations from the input layer to the output layer (feedforward) and then calculating the slope of the loss function from the output layer to the input layer. The structure of the neural network (NN) model consists of several hidden layers between the input and the output, and the output is predicted according to the input by giving nonlinear characteristics between the design variables and the output. A function that converts the weighted sum of input data into an output signal is called an activation function. The rectified linear unit (ReLU) function, which can supplement the gradient vanishing of the sigmoid function, is used as the activation function. The ReLU function outputs 0 if the input value is less than 0 and outputs the input value if it is greater than 0, as expressed in Equation (3).

$$f(x) = \begin{cases} x\ (x > 0) \\ 0\ (x < 0) \end{cases} \tag{3}$$

In this study, input variables of the neural network model were set as the five geometrical variables to make a model for predicting oil–water separation efficiency (η). The separation efficiency is defined as the ratio of the oil mass flow rate through LPO to the oil mass flow rate at the inlet. The separation efficiency can be calculated by Equation (4) as follows:

$$\eta = \frac{Q_{LPO.oil}}{Q_{inlet.\ oil}} \tag{4}$$

Design points for developing neural network models were created based on the design-of-experiments (DOE) method. This method has the advantage of creating a design area where a considerable amount of information can be obtained, and the Latin hypercube sampling (LHS) method [42] was used. Table 2 shows the design points generated using DOE. The machine learning model was trained and evaluated using the numerical results for these design points. In addition, the neural network of the machine learning model has hyperparameters such as the learning rate, number of the hidden layer, number of nodes in the hidden layer, etc. Additionally, an optimization study is needed to reduce the error of the prediction value. In this study, hyperparameter optimization was performed on the

number of hidden layers, the number of nodes in each hidden layer, and the learning rate, and Python was used for the machine learning model and hyperparameter optimization.

Table 2. Design points of LHS.

Design Point	Conical Diameter (D_1) [mm]	Conical Length (L_1) [mm]	Number of Vanes (n)	Angle of Vane (θ) [°]	Thickness of Vane (t) [mm]
Training set					
1	48.00	500	9	65.00	3.0
2	41.93	420	5	46.70	2.6
3	42.22	461	7	72.20	2.9
4	40.15	502	8	66.70	2.3
5	47.85	543	6	73.30	3.1
6	46.37	583	7	60.00	2.3
7	46.96	624	7	50.00	3.4
8	42.52	665	7	64.40	4.0
9	41.33	706	8	51.10	3.7
10	47.26	746	7	47.80	3.8
11	47.56	787	8	68.90	2.7
12	43.11	828	7	57.80	2.1
13	45.48	869	8	55.60	3.4
14	41.04	909	9	61.10	3.5
15	43.70	950	6	65.60	2.8
16	46.67	991	9	53.30	2.2
17	40.74	1031	6	45.60	2.4
18	44.30	1072	8	71.10	2.9
19	46.07	1113	8	48.90	3.0
20	40.44	1154	6	67.80	2.6
21	45.78	1194	6	62.20	3.3
22	44.89	1235	5	63.30	3.2
23	44.00	1276	5	52.20	3.9
Test set					
24	41.63	1317	9	56.70	3.6
25	42.81	1357	6	70.00	3.1
26	44.59	1398	8	74.40	3.7
27	43.41	1439	7	54.40	2.5
28	45.19	1480	6	58.90	2.0

4. Results and Discussion

4.1. Results of Computational Fluid Dynamics

To ensure an accurate numerical simulation, the simulation results are usually associated with those of similar previous validated numerical studies. The numerical calculation results in this study were compared with the calculation and experimental results by Slot et al. [22]. Figure 5 shows the result of comparing the axial velocity at a distance of 0.44 m from the swirl generator. The trend of predicted axial velocity in both studies, numerical results of Slot et al. [22] and the present study, is identical, with a mean deviation below 15%, which denotes an acceptable agreement. The maximum deviation was found to be r/D 0.31. This deviation is considered to be caused by the difference in the geometry of the separator, the size of the incoming oil droplet, and the grid system.

Table 3 shows the CFD results by design points. Figure 6 shows the tangential velocity at a distance of 2D downstream of the ISE. Figure 7 shows the distribution of tangential velocity at six vanes of the swirl generator. The maximum tangential velocity appears in the exit region of the vane. As the angle of vane increased, the magnitude of the maximum tangential velocity increased, and the position of the maximum tangential velocity tended to be closer to the wall of the separator. The two regions of the forced vortex and free vortex can be divided into points with maximum tangential velocity. This appears similar to the

Rankine vortex structure [43]. In the forced vortex region, the tangential velocity appeared proportional to the radius, and in the free vortex region, the tangential velocity decreased along the radius. The tangential velocity rapidly decreased near the wall, because of the wall friction. In addition, the maximum tangential velocity was found to be faster, as the vane angle of the swirl generator was larger.

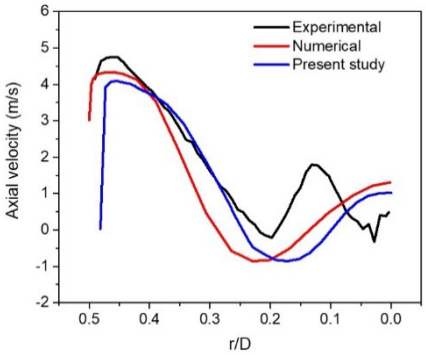

Figure 5. Comparison of axial velocity with the experiment and numerical analysis results [22].

Table 3. Numerical calculation results for design points.

Design Point	Conical Diameter (D_1) [mm]	Conical Length (L_1) [mm]	Number of Vanes (n)	Angle of Vane (θ) [°]	Thickness of Vane (t) [mm]	Pressure Drop [kPa]	Separation Efficiency
Training set							
1	48.00	500	9	65.00	3.0	193.64	0.876
2	41.93	420	5	46.70	2.6	48.58	0.809
3	42.22	461	7	72.20	2.9	324.72	0.814
4	40.15	502	8	66.70	2.3	212.50	0.804
5	47.85	543	6	73.30	3.1	264.88	0.884
6	46.37	583	7	60.00	2.3	94.31	0.823
7	46.96	624	7	50.00	3.4	60.65	0.813
8	42.52	665	7	64.40	4.0	190.94	0.816
9	41.33	706	8	51.10	3.7	89.46	0.824
10	47.26	746	7	47.80	3.8	55.56	0.809
11	47.56	787	8	68.90	2.7	223.83	0.874
12	43.11	828	7	57.80	2.1	88.25	0.810
13	45.48	869	8	55.60	3.4	97.37	0.821
14	41.04	909	9	61.10	3.5	186.00	0.828
15	43.70	950	6	65.60	2.8	134.09	0.827
16	46.67	991	9	53.30	2.2	74.38	0.818
17	40.74	1031	6	45.60	2.4	51.97	0.825
18	44.30	1072	8	71.10	2.9	312.04	0.864
19	46.07	1113	8	48.90	3.0	61.21	0.815
20	40.44	1154	6	67.80	2.6	166.09	0.826
21	45.78	1194	6	62.20	3.3	107.35	0.831
22	44.89	1235	5	63.30	3.2	95.39	0.838
23	44.00	1276	5	52.20	3.9	57.50	0.816
Test set							
24	41.63	1317	9	56.70	3.6	132.23	0.830
25	42.81	1357	6	70.00	3.1	203.36	0.835
26	44.59	1398	8	74.40	3.7	610.18	0.892
27	43.41	1439	7	54.40	2.5	74.25	0.820
28	45.19	1480	6	58.90	2.0	75.07	0.826

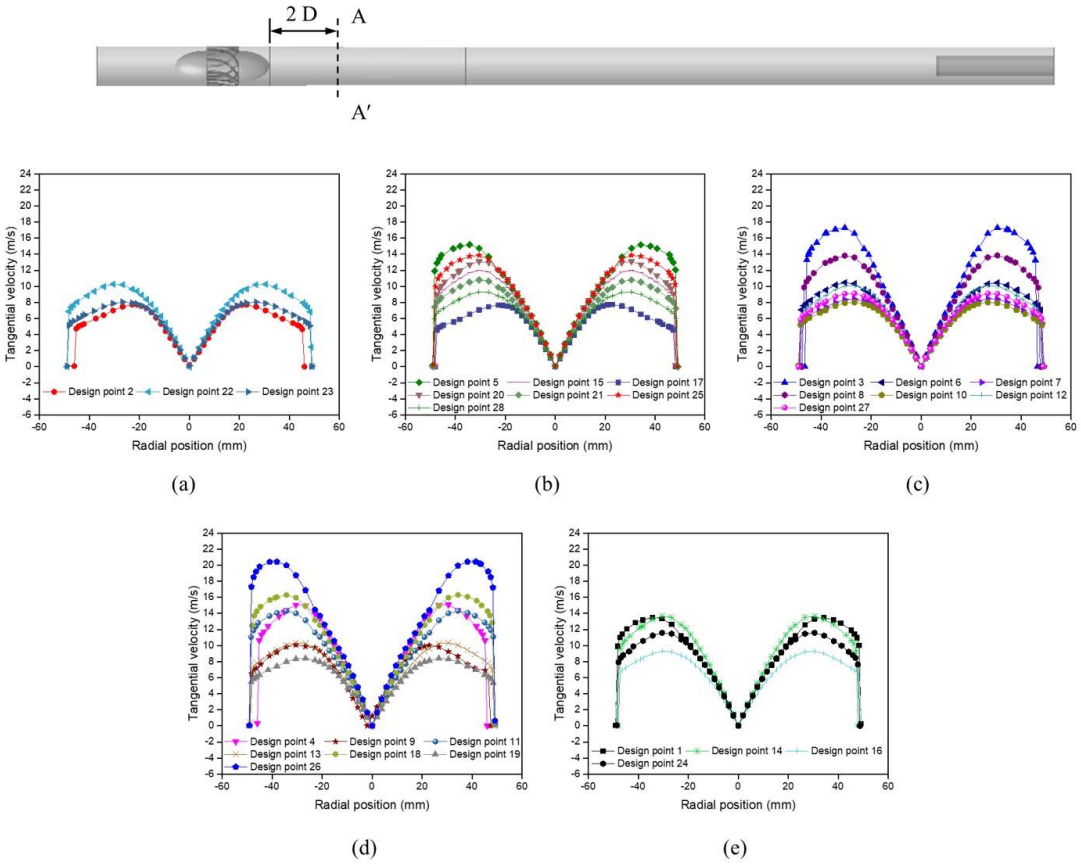

Figure 6. Tangential velocity at 2D downstream of the ISE: (**a**) at 5 vanes, (**b**) at 6 vanes, (**c**) at 7 vanes, (**d**) at 8 vanes, and (**e**) at 9 vanes.

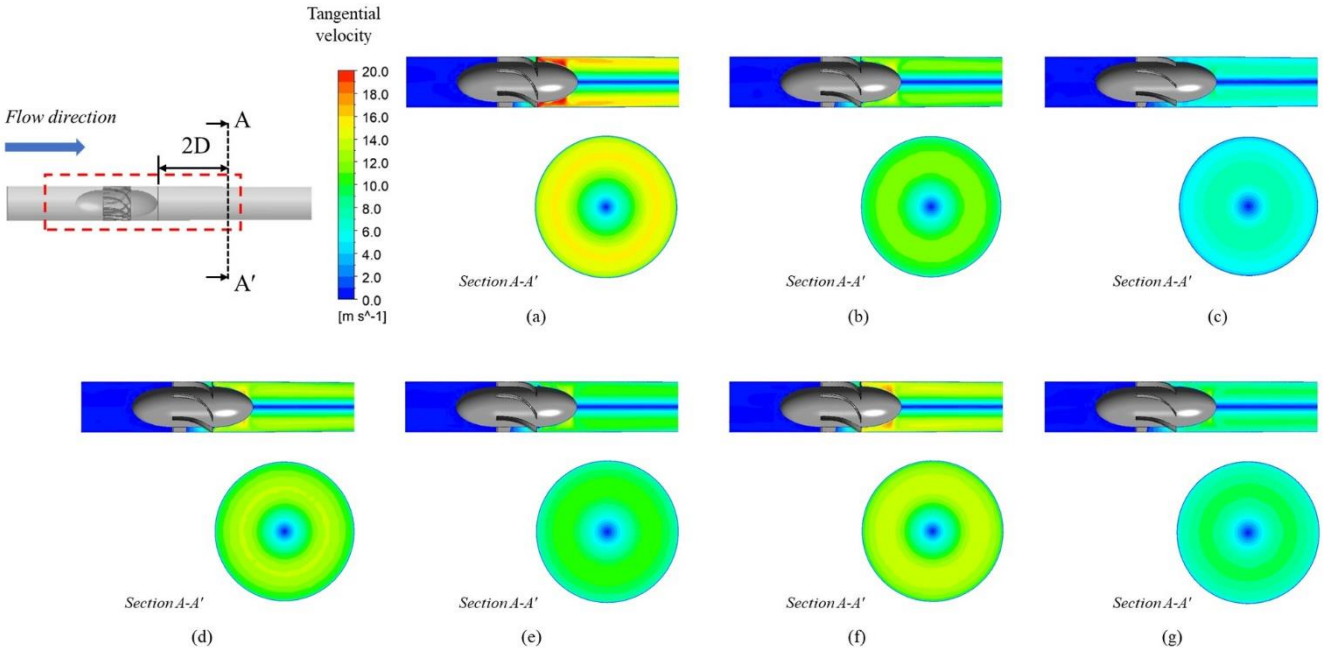

Figure 7. Distribution of tangential velocity at six vanes: Design point 5 (**a**), 15 (**b**), 17 (**c**), 20 (**d**), 21 (**e**), 25 (**f**), 28 (**g**).

Pearson correlation coefficient (PCC) [44] was used to evaluate the effect of geometrical variables on oil–water separation efficiency. The Pearson correlation coefficient quantifies the linear correlation between the random variable X and the output Y and is expressed as a value between −1 and +1. A Pearson correlation coefficient of 1 indicates a perfect positive linear correlation between two variables, a value of −1 indicates a perfect negative linear correlation, and a value of 0 indicates no linear relationship. Figure 8 is a PCC matrix heatmap showing the effect of geometrical variables on the separation efficiency. The effect on the separation efficiency was shown in the order of angle of the vane, conical diameter, and the number of vanes.

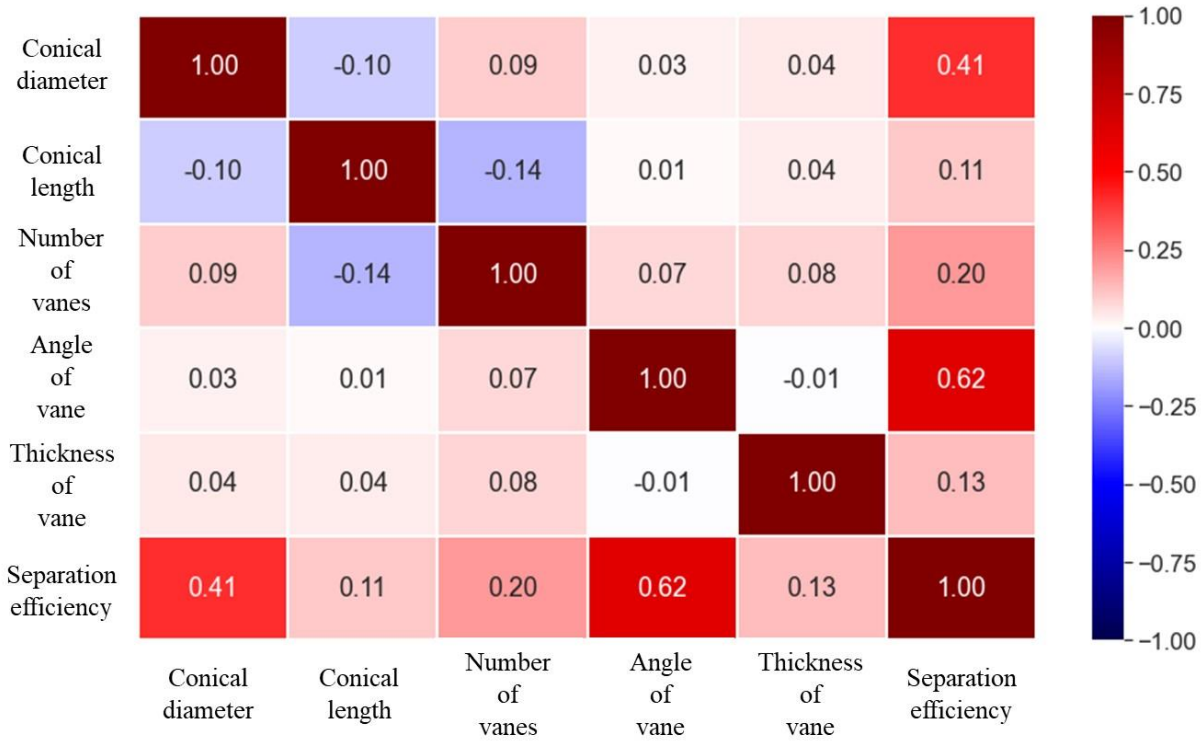

Figure 8. Pearson correlation coefficient heat map of separation efficiency between five design parameters.

Figure 9a shows the results for the pressure drop and separation efficiency, with the pressure drop defined as the pressure difference between the inlet and HPO. The separation efficiency tended to increase as the pressure drop increased, and as shown in Figure 9b, the magnitude of the pressure drop tended to be greater with the increase in the angle of the vane (θ). The large vane angle induced a strong swirl, so a larger shear loss likely occurred in the wall of the separator.

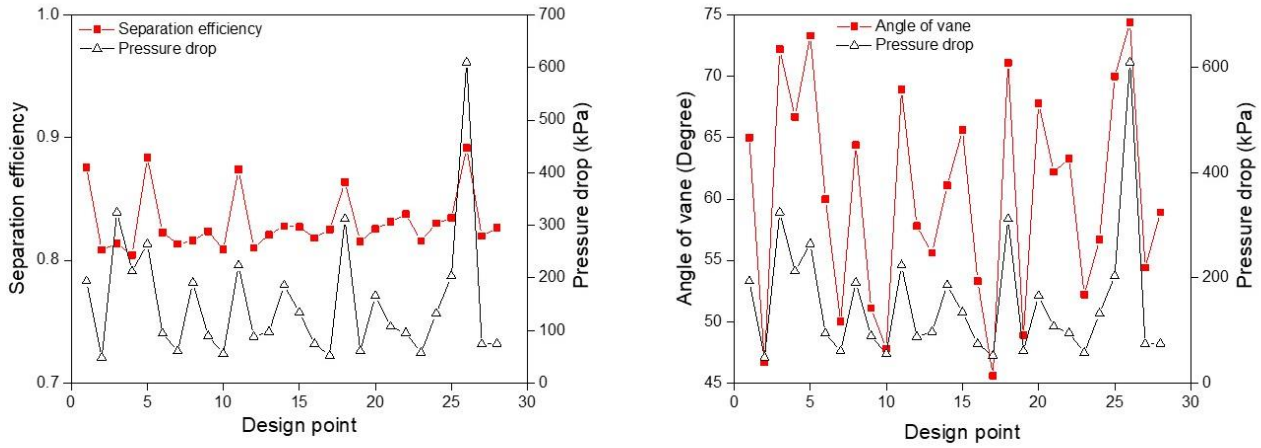

(a) (b)

Figure 9. Results of the numerical calculation: (**a**) Separation efficiency and pressure drop for all design point, (**b**) Angle of vane and pressure drop for all design point.

4.2. Separation Efficiency Prediction Model Development Using Neural Network Algorithm

A neural network method was used to develop a prediction model for the separation efficiency of the axial oil–water separator. The prediction performance of neural network algorithms depends on hyperparameters, and hyperparameter optimization is required to develop a prediction model. In this study, the number of hidden layers constituting the neural network, the number of nodes in the hidden layer, and the learning rate were used as hyperparameters. Depending on the number of hidden layers and the number of nodes in the hidden layer, an overfitting problem can occur or consume considerable learning time, so it is necessary to determine the optimal number of hidden layers and nodes. The learning rate refers to the amount to learn when updating the model's weights. A random sampling method was used to derive the optimal hyperparameter, and the number of sampling was set to 500. Feature scaling was performed with min–max normalization for input variables of different sizes. Ridge regularization was used to prevent overfitting the model by keeping the model weights as small as possible. Figure 10 shows the hyperparameter optimization results. The right end of Figure 10 is the quantification of the prediction performance according to the hyperparameter combination. Mean absolute error (MAE), mean absolute percentage error (MAPE), and R square (R^2) were used as indicators for quantitative evaluation of the model. MAE is an index that indicates the difference between the predicted value and the actual value and is an index that can objectively evaluate the performance of a neural network model. MAPE is the percentage of MAE. It is widely used as an evaluation indicator for predictive models and has the advantage of scale independence. The closer the MAPE value is to 0, the more the predicted value matches the actual value. R^2 is an indicator of the degree of agreement between the actual value and the predicted value. The closer the R^2 value is to 1, the more the predicted value matches the actual value. Table 4 shows the optimal hyperparameter combinations.

Based on the optimal hyperparameter, CFD calculation results were divided into train set and test set to develop and evaluate a neural network model. MLR results were compared to evaluate the performance of neural network models. Figure 11 shows the prediction results of the neural network model and the MLR model. Since complex nonlinear relationships occur between design variables and separation efficiency of oil-water separators, the neural network model shows better prediction results than the MLR model. Table 5 shows quantitative indicators of predictive models. As a result of the neural network model prediction, the model performance was improved by about 79.2%, 71.9% and 74.0%, respectively, in MAE, MAPE and R^2 compared to the MLR model.

Table 4. The optimized hyperparameters.

Optimized Parameters	Value
Learning rate	0.09883
Number of hidden layers	6
Number of nodes	28/32/28/16/28/12

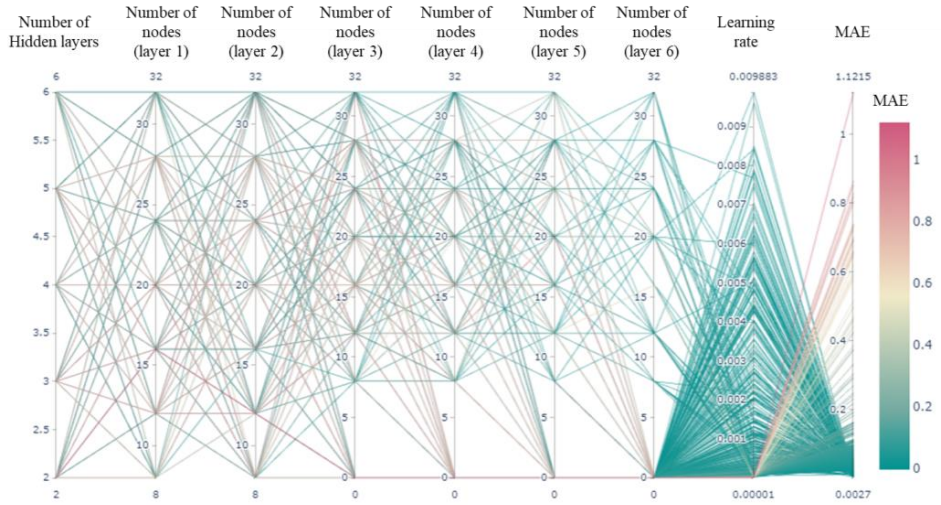

Figure 10. Hyperparameter tuning results.

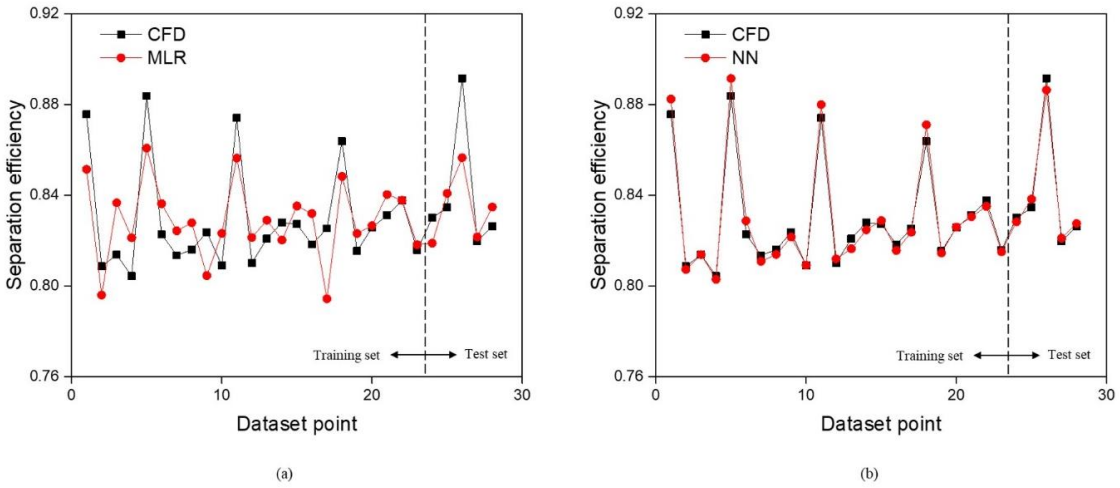

Figure 11. The training results and prediction results by the NN and MLR: (**a**) Multi linear regression results, (**b**) Neural network results.

Table 5. Neural network prediction model performance, compared with MLR results.

	MLR Model	Neural Network Model	Improvement
MAE	0.0129	0.00268	79.2%
MAPE	0.0146	0.0041	71.9%
R^2	0.566	0.985	74.0%

5. Conclusions

In this paper, a neural network model was developed to analyze the effect of various design variables on the separation performance of an axial-flow oil–water separator and to predict the separation performance. The following conclusions are drawn:

(1) Among the various design variables, the effect of vane angle on the separation performance of axial oil–water separator was significant. When the value of the vane angle was large, the efficiency was relatively high, and it was confirmed that the magnitude of the pressure drop was also large.
(2) The neural network model was developed using the CFD results for the design points created by the DOE method. Hyperparameter optimization was performed, and the neural network prediction model improved about 79.2% in MAE, 71.9% in MAPE, and 74% in R^2, compared with the traditional MLR. Therefore, the neural network model using the CFD results can be efficiently applied to the design of the axial-flow oil–water separator.

In a future study, a more accurate neural network model will be developed through various hyperparameter optimization methods, and a separation performance prediction model using various boundary conditions such as inlet and outlet will be investigated.

Author Contributions: Conceptualization, Y.-W.J., Y.-J.K. (Young-Ju Kim) and Y.-J.K. (Youn-Jea Kim); methodology, Y.-W.J.; software, Y.-W.J.; validation, Y.-W.J.; formal analysis, Y.-W.J.; investigation, Y.-W.J.; resources, Y.-W.J. and Y.-J.K. (Young-Ju Kim); data curation, Y.-W.J.; writing—original draft preparation, Y.-W.J. and Y.-J.K. (Youn-Jea Kim); writing—review and editing, Y.-W.J. and Y.-J.K. (Youn-Jea Kim); supervision, Y.-J.K. (Youn-Jea Kim). All authors have read and agreed to the published version of the manuscript.

Funding: This research is supported by the Korea Agency for Infrastructure Technology Advancement (KAIA) grant funded by the Ministry of Land, Infrastructure, and Transport (Grant 22DPRB-C162320-02).

Institutional Review Board Statement: Not applicable.

Informed Consent Statement: Not applicable.

Data Availability Statement: The data presented in this study are available on request from the corresponding author.

Conflicts of Interest: The authors declare no conflict of interest.

Nomenclature

D	Diameter of separator inlet
D_1	Diameter of the conical section
D_{sg}	Diameter of the swirl generator
$\vec{F}$	The body force
$\vec{g}$	The gravity acceleration
L_1	Length of the conical section
L_2	Length of cylinder section at downstream
L_{nose}	Length of swirl generator nose section
L_{vane}	Length of swirl generator vane section
L_{tail}	Length of swirl generator tail section
n	Number of swirl generator vanes
$Q_{LPO.oil}$	Mass flow rate of oil at LPO
$Q_{inlet.oil}$	Mass flow rate of oil at the inlet
t	Thickness of vane
$\vec{v}_{dr}$	The drift velocity
$\vec{v}_m$	The mixture velocity
θ	Angle of vane
η	Separation efficiency
ρ_m	The mixture density
μ_m	The viscosity of the mixture
α	The volume fraction

References

1. Wang, B.; Xu, D.; Chu, K.; Yu, A. Numerical study of gas–solid flow in a cyclone separator. *Appl. Math. Model.* **2006**, *30*, 1326–1342. [CrossRef]
2. Chu, K.W.; Wang, B.; Xu, D.L.; Chen, Y.X.; Yu, A.B. CFD-DEM simulation of the gas-solid flow in a cyclone separator. *Chem. Eng. Sci.* **2011**, *66*, 834–847. [CrossRef]
3. Klujszo, L.A.; Rafaelof, M.; Rajamani, R.K. Dust collection performance of a swirl air cleaner. *Powder Technol.* **1999**, *103*, 130–138. [CrossRef]
4. Zhou, H.; Hu, Z.; Zhang, Q.; Wang, Q.; Lv, X. Numerical study on gas-solid flow characteristics of ultra-light particles in a cyclone separator. *Powder Technol.* **2019**, *344*, 784–796. [CrossRef]
5. Hoekstra, A.J. Gas Flow Field and Collection Efficiency of Cyclone Separators. Ph.D. Thesis, Delft University of Technology, Delft, The Netherlands, 2000.
6. Mikulčić, H.; Vujanović, M.; Ashhab, M.S.; Duić, N. Large eddy simulation of a two-phase reacting swirl flow inside a cement cyclone. *Energy* **2014**, *75*, 89–96. [CrossRef]
7. Liu, W.; Bai, B. Swirl decay in the gas–liquid two-phase swirling flow inside a circular straight pipe. *Exp. Therm. Fluid Sci.* **2015**, *68*, 187–195. [CrossRef]
8. Xiong, Z.; Lu, M.; Wang, M.; Gu, H.; Cheng, X. Study on flow pattern and separation performance of air–water swirl-vane separator. *Ann. Nucl. Energy* **2014**, *63*, 138–145. [CrossRef]
9. Rocha, A.D.; Bannwart, A.C.; Ganzarolli, M.M. Numerical and experimental study of an axially induced swirling pipe flow. *Int. J. Heat Fluid Flow* **2015**, *53*, 81–90. [CrossRef]
10. Huang, L.; Deng, S.; Chen, Z.; Guan, J.; Chen, M. Numerical analysis of a novel gas-liquid pre-separation cyclone. *Sep. Purif. Technol.* **2018**, *194*, 470–479. [CrossRef]
11. Hreiz, R.; Gentric, C.; Midoux, N.; Lainé, R.; Fünfschilling, D. Hydrodynamics and velocity measurements in gas–liquid swirling flows in cylindrical cyclones. *Chem. Eng. Res. Des.* **2014**, *92*, 2231–2246. [CrossRef]
12. Swanborn, R.A. A New Approach to the Design of Gas-Liquid Separators for the Oil Industry. Ph.D. Thesis, Delft University of Technology, Delft, The Netherlands, 1988.
13. Yue, T.; Chen, J.; Song, J.; Chen, X.; Wang, Y.; Jia, Z.; Xu, R. Experimental and numerical study of Upper Swirling Liquid Film (USLF) among Gas-Liquid Cylindrical Cyclones (GLCC). *Chem. Eng. J.* **2019**, *358*, 806–820. [CrossRef]
14. Wang, G.; Yan, C.; Fan, G.; Wang, J.; Xu, J.; Zeng, X.; Liu, A. Experimental study on a swirl-vane separator for gas–liquid separation. *Chem. Eng. Res. Des.* **2019**, *151*, 108–119. [CrossRef]
15. Liu, L.; Wang, K.; Bai, B. Experimental study on flow patterns and transition criteria for vertical swirling gas-liquid flow. *Int. J. Multiph. Flow* **2020**, *122*, 103113. [CrossRef]
16. Delfos, R.; Murphy, S.; Stanbridge, D.; Olujic, D.; Jansens, P.J. A design tool for optimising axial liquid–liquid hydrocyclones. *Miner. Eng.* **2004**, *17*, 721–731. [CrossRef]
17. Amini, S.; Mowla, D.; Golkar, M. Developing a new approach for evaluating a de-oiling hydrocyclone efficiency. *Desalination* **2012**, *285*, 131–137. [CrossRef]
18. Huang, S. Numerical Simulation of Oil-water Hydrocyclone Using Reynolds-Stress Model for Eulerian Multiphase Flows. *Can. J. Chem. Eng.* **2008**, *83*, 829–834. [CrossRef]
19. Yaojun, L.; Lixing, Z.; Xiong, S. Numerical simulation of strongly swirling turbulent flows in a liquid-liquid hydrocyclone using the Reynolds stress transport equation model. *Sci. China* **2000**, *43*, 86–96.
20. Husveg, T.; Rambeau, O.; Drengstig, T.; Bilstad, T. Performance of a deoiling hydrocyclone during variable flow rates. *Miner. Eng.* **2007**, *20*, 368–379. [CrossRef]
21. Campen, L.V.; Mudde, R.F.; Slot, J.J.; Hoeihmakers, H. A numerical and experimental survey of a liquid-liquid axial cyclone. *Int. J. Chem. React. Eng.* **2012**, *10*, A35. [CrossRef]
22. Slot, J.J.; Campen, L.V.; Hoeijmakers, H.; Mudde, R.F. In-line oil-water separation in swirling flow. In Proceedings of the 8th International Conference on CFD in Oil & Gas, Metallurgical and Process Industries, Trondheim, Norway, 21–23 June 2011.
23. Oropeza-Vazquez, C.; Afanador, E.; Gomez, L.; Wang, S.; Mohan, R.; Shoham, O.; Kouba, G. Oil-water separation in a novel liquid-liquid cylindrical cyclone (LLCC) compact separator-Experiments and modeling. In Proceeding of ASME FEDSM'03, Honolulu, HI, USA, 6–10 July 2003; FEDSM2003-45547.
24. Zeng, X.; Zhao, L.; Fan, G.; Yan, C. Numerical and experimental study on a new axial separator for liquid-liquid separation. *J. Taiwan Inst. Chem. Eng.* **2021**, *123*, 104–114. [CrossRef]
25. Sharifi, K.; Behnahani, T.J.; Ebrahimi, S.; Sabeti, M.; Soflaee, S. A new computational fluid dynamics study of a liquid-liquid hydrocyclone in the two phase case for separation of oil droplets and water. *Braz. J. Chem. Eng.* **2019**, *36*, 1601–1612. [CrossRef]
26. Noroozi, S.; Hashemabadi, S.H. CFD Simulation of Inlet Design Effect on Deoiling Hydrocyclone Separation Efficiency. *Chem. Eng. Technol.* **2009**, *32*, 1885–1893. [CrossRef]
27. Zeng, X.; Zhao, L.; Zhao, W.; Hou, M.; Zhu, F.; Fan, G.; Yan, C. Experimental study on a compact axial separator with conical tube for liquid-liquid separation. *Sep. Purif. Technol.* **2021**, *257*, 117904. [CrossRef]
28. Schütz, S.; Gorbach, G.; Piesche, M. Modeling fluid behavior and droplet interactions during liquid–liquid separation in hydrocyclones. *Chem. Eng. Sci.* **2009**, *64*, 3935–3952. [CrossRef]

29. Young, G.; Wakley, W.; Taggart, D.; Andrews, S.; Worrell, J. Oil-water separation using hydrocyclones: An experimental search for optimum dimensions. *J. Pet. Sci. Eng.* **1994**, *11*, 37–50. [CrossRef]
30. Al-Kayiem, H.H.; Hamza, J.E.; Lemmu, T.A. Performance enhancement of axial concurrent liquid–liquid hydrocyclone separator through optimization of the swirler vane angle. *J. Pet. Explor. Prod. Technol.* **2020**, *10*, 2957–2967. [CrossRef]
31. Zeng, X.; Xu, Y.; Zhao, L.; Fan, G.; Yan, C. Numerical investigation on axial liquid-liquid separators with different swirl chambers. *Chem. Eng. Process. Process Intensif.* **2021**, *161*, 108324. [CrossRef]
32. Elsayed, K.; Lacor, C. Modeling and Pareto optimization of gas cyclone separator performance using RBF type artificial neural networks and genetic algorithms. *Powder Technol.* **2012**, *217*, 84–99. [CrossRef]
33. Safikhani, H. Modeling and multi-objective Pareto optimization of new cyclone separators using CFD, ANNs and NSGA II algorithm. *Adv. Powder Technol.* **2016**, *27*, 2277–2284. [CrossRef]
34. Park, D.; Cha, J.; Kim, M.; Go, J.S. Multi-objective optimization and comparison of surrogate models for separation performances of cyclone separator based on CFD, RSM, GMDH-neural network, back propagation-ANN and genetic algorithm. *Eng. Appl. Comput. Fluid Mech.* **2019**, *14*, 180–201. [CrossRef]
35. Wang, S.; Wang, D.; Yang, Y.; Zhang, X. Phase-isolation of upward oil–water flow using centrifugal method. *Flow Meas. Instrum.* **2015**, *46*, 33–43. [CrossRef]
36. Grady, S.; Wesson, G.; Abdullah, M.; Kalu, E. Prediction of 10-mm Hydrocyclone Separation Efficiency Using Computational Fluid Dynamics. *Filtr. Sep.* **2003**, *40*, 41–46. [CrossRef]
37. Ishii, M.; Zuber, N. Drag coefficient and relative velocity in bubbly, droplet or particulate flows. *AIChE J.* **1979**, *25*, 843–855. [CrossRef]
38. Avci, A.; Karagoz, I.; Surmen, A. Development of a new method for evaluating vortex length in reversed flow cyclone separators. *Powder Technol.* **2013**, *235*, 460–466. [CrossRef]
39. Wang, J.; Bai, Z.; Yang, Q.; Fan, Y.; Wang, H. Investigation of the simultaneous volumetric 3-component flow field inside a hydrocyclone. *Sep. Purif. Technol.* **2016**, *163*, 120–127. [CrossRef]
40. Yang, I.; Shin, H.; Kim, C.B.; Kim, T.H. A tree-dimensional simulation of a hydrocyclone for the sludge separation in water purifying plants and comparison with experimental data. *Miner. Eng.* **2004**, *17*, 637–641. [CrossRef]
41. Cai, B.; Wang, J.; Sun, L.; Zhang, N.; Yan, C. Experimental study and numerical optimization on a vane-type separator for bubble separation in TMSR. *Prog. Nucl. Energy* **2014**, *74*, 1–13. [CrossRef]
42. McKay, M.D.; Beckman, R.J.; Conover, W.J. A comparison of three methods for selecting values of input variables in the analysis of output from a computer code. *Technometrics* **2000**, *42*, 55–61. [CrossRef]
43. Rankine, W.J.M. *A Manual of Applied Mechanics*; Charles Griffin and Co.: London, UK, 1877.
44. Pearson, K. VII. Mathematical contributions to the theory of evolution—III. Regression, heredity, and panmixia. *Philos. Trans. R. Soc. Lond. Ser. Contain. Pap. Math. Phys. Character* **1896**, *187*, 253–318. [CrossRef]